ORCA – Online Research @ Cardiff

This is an Open Access document downloaded from ORCA, Cardiff University's institutional repository:https://orca.cardiff.ac.uk/id/eprint/119425/

This is the author’s version of a work that was submitted to / accepted for publication.

Citation for final published version:

Dann, Ellie K., Gibson, Emma K., Blackmore, Rachel H., Catlow, C. Richard A. , Collier, Paul, Chutia, Arunabhiram, Erden, Tugce Eralp, Hardacre, Christopher, Kroner, Anna, Nachtegaal, Maarten, Raj, Agnes, Rogers, Scott M., Taylor, S. F. Rebecca, Thompson, Paul, Tierney, George F., Zeinalipour-Yazdi, Constantinos D., Goguet, Alexandre and Wells, Peter P. 2019. Structural selectivity of supported Pd nanoparticles for catalytic NH3 oxidation resolved using combined operando spectroscopy. Nature Catalysis 2 , pp. 157-163. 10.1038/s41929-018-0213-3

Publishers page: http://dx.doi.org/10.1038/s41929-018-0213-3

Please note:
Changes made as a result of publishing processes such as copy-editing, formatting and page numbers may not be reflected in this version. For the definitive version of this publication, please refer to the published source. You are advised to consult the publisher’s version if you wish to cite this paper.

This version is being made available in accordance with publisher policies. See http://orca.cf.ac.uk/policies.html for usage policies. Copyright and moral rights for publications made available in ORCA are retained by the copyright holders.

Structural selectivity of supported Pd nanoparticles for catalytic NH_3 oxidation resolved using combined operando spectroscopy

Ellie K. Dann[1,2], Emma K. Gibson[2,3], Rachel H. Blackmore[2,4], C. Richard A. Catlow[1,2,5], Paul Collier[6], Arunabhiram Chutia[2,7], Tugce Eralp Erden[6], Christopher Hardacre[2,8], Anna Kroner[9], Maarten Nachtegaal[10], Agnes Raj[6], Scott M. Rogers[1,2], S. F. Rebecca Taylor[8], Paul Thompson[11], George F. Tierney[2,4], Constantinos D. Zeinalipour-Yazdi[2,12], Alexandre Goguet[2,13]* and Peter P. Wells[2,4,9]*

The selective catalytic oxidation of NH_3 to N_2 presents a promising solution for the abatement of unused NH_3-based reductants from diesel exhaust after treatment. Supported Pd nanoparticle catalysts show selectivity to N_2 rather than NO_x, which is investigated in this work. The link between Pd nanoparticle structure and surface reactivity was found using operando X-ray absorption fine structure spectroscopy, diffuse reflectance infrared Fourier-transformed spectroscopy and on-line mass spectrometry. Nitrogen insertion into the metallic Pd nanoparticle structure at low temperatures (<200 °C) was found to be responsible for high N_2 selectivity, whereas the unfavourable formation of NO is linked to adsorbed nitrates, which form at the surface of bulk PdO nanoparticles at high temperatures (>280 °C). Our work demonstrates the ability of combined operando spectroscopy and density functional theory calculations to characterize a previously unidentified PdN_x species, and clarify the selectivity-directing structure of supported Pd catalysts for the selective catalytic oxidation of NH_3 to N_2.

The selective catalytic oxidation of ammonia (NH_3-SCO) is needed to eliminate the slip of unreacted NH_3 from automotive exhausts. NH_3 is used as the reductant for the selective catalytic reduction (NH_3-SCR) of harmful nitrogen oxides (NO_x) that are released from diesel engines. NH_3 slip from these exhaust systems is increasing as legislation pushes for greater efficiency of de-NO_x technology, which is achieved using greater amounts of the NH_3 reductant. High-performance catalysts for the NH_3-SCO reaction downstream of NH_3-SCR must be able to achieve complete conversion of NH_3 to N_2 and H_2O, at low temperatures (T <400 °C) and without the reformation of harmful NO_x.

Noble metals supported on metal oxides have repeatedly been found to possess high catalytic activity for NH_3 oxidation at low temperatures, but over-oxidation to nitrogen oxides is problematic[1–7]. Various attempts to improve the selectivity and avoid the use of noble metals have investigated the use of base metal oxides and transition metal ion-exchanged zeolites[8–10]. However, even the more selective of these catalysts, CuO[11,12] and V_2O_5[13], have lacked sufficient activity to be of practical use[14]. Of all the noble metals, the most promising N_2 selectivity is found for Pd-based catalysts[15]. Various studies with Pd catalysts have examined the incorporation of Pd into multicomponent metal systems[3,16], mixed metal oxide perovskite materials[17], the use of various supports[18] and varying metal loading[19], concluding that Pd nanoparticles are the active species irrespective of the support[19,20]. Despite these studies, there remains little understanding of the fundamental chemistry that governs the catalytic activity of Pd nanoparticles for NH_3-SCO.

The use of Pd nanoparticles in catalysis is well established, and it is accepted that the Pd nanoparticle structure can change under different reaction environments. For example, the bulk oxidation and reduction of Pd nanoparticles is demonstrated by switching the oxygen-to-fuel ratio during lean/rich methane oxidation[21]. The formation of palladium hydrides and carbides is also reported during operation of hydrogenation reactions, and these are found to affect the catalytic performance[22–24]. However, there is a lack of evidence regarding the noble metal structure and speciation for the NH_3-SCO reaction. Zhang et al. have suggested that the oxidation state of the precious metal catalyst influences the NH_3-SCO activity, but without in situ measurements it is difficult to draw definite conclusions[25]. Furthermore, there is no explanation for the increasing formation of nitrogen oxides at higher temperatures[20].

These problems highlight the importance of in situ methods in studying the catalyst under real working environments. The high energy of the Pd K edge (24,357 eV) is advantageous for in situ and operando X-ray absorption fine structure spectroscopy (XAFS), which is able to penetrate the reaction medium and probe the 1*s* to 4*p* electronic transitions of Pd atoms in the supported nanoparticle catalysts. X-rays at the Pd L_3 edge (3,173 eV) have lower penetrating

---

[1] Department of Chemistry, University College London, London, UK. [2] UK Catalysis Hub, Research Complex at Harwell, Rutherford Appleton Laboratory, Didcot, UK. [3] School of Chemistry, University of Glasgow, Glasgow, UK. [4] School of Chemistry, University of Southampton, Southampton, UK. [5] Cardiff Catalysis Institute, School of Chemistry, Cardiff University, Cardiff, UK. [6] Johnson Matthey Technology Centre, Sonning Common, Reading, UK. [7] School of Chemistry, University of Lincoln, Lincoln, UK. [8] School of Chemical Engineering & Analytical Science, The University of Manchester, Manchester, UK. [9] Diamond Light Source, Didcot, UK. [10] Paul Scherrer Institute, Villigen, Switzerland. [11] XMaS (the UK CRG Beamline), European Synchrotron Radiation Facility, Grenoble, France. [12] School of Science, University of Greenwich, Chatham Maritime, UK. [13] School of Chemistry and Chemical Engineering, Queen's University Belfast, Belfast, UK. *e-mail: a.goguet@qub.ac.uk; ppwells@soton.ac.uk

power, but can also be used under carefully controlled in situ condi-tions to probe the 2*p*–4*d* electronic transitions, giving information regarding the empty *d* density of states, which is crucial for distin-guishing between hydride, carbide and other potential phases[26]. Diffuse reflectance infrared Fourier-transform spectroscopy (DRIFTS) may also be applied as a complementary in situ method, to provide information for the reaction mechanism by probing molecular vibrations of adsorbed intermediates at the catalyst surface.

In this study, two high-performance supported Pd nanoparticle catalysts (Pd/γ-Al_2O_3 and Pd/zeolite-Y) are investigated for NH_3-SCO using a combination of XAFS with DRIFTS and on-line mass spectrometry. By performing simultaneous XAFS and DRIFTS of the catalyst under operating conditions, links between bulk nanoparticle structure, reaction mechanisms and catalytic activity are revealed, which are also supported by our theoretical calcula-tions based on density functional theory and dispersion corrections (DFT +D3). In this way, not only have we identified the Pd struc-tural changes and formation of a previously unidentified palladium nitride, which occur within the temperature range for NH_3-SCO, but we can also correlate these with the change in surface speciation, catalytic reactivity and product distribution.

Results

Ex situ characterization. Two supported 1.5 wt% Pd catalysts were prepared by incipient wetness impregnation. Pd K-edge X-ray absorption near-edge structure spectroscopy (XANES) of the sup-ported Pd catalysts after impregnation and calcination were consis-tent with that of bulk PdO (Supplementary Fig. 1). Transmission electron microscopy (TEM) images of the as-prepared catalysts show PdO nanoparticles supported on γ-Al_2O_3 (Supplementary Fig. 2) and zeolite-Y (Supplementary Fig. 3). PdO nanoparticles can be observed as dark spots contrasted against the support, which appear to have a smaller average particle size when supported on γ-Al_2O_3 compared with zeolite-Y.

After a reduction pre-treatment in 10% H_2/He, the Pd K-edge XANES of the supported Pd catalysts can be matched to that of Pd foil (Supplementary Fig. 4), with small differences attributed to particle size and temperature effects[27]. By fitting the Fourier-transformed Pd K-edge EXAFS spectra of the reduced catalysts (Supplementary Fig. 5 and Supplementary Table 1) to a model using a single Pd–Pd scattering path, the Pd coordination numbers of Pd/γ-Al_2O_3 and Pd/zeolite-Y were found to be 9.7 and 11.3, respec-tively. These values correspond to average particle diameters of 2.1 and 5.2 nm, respectively (as calculated using a method reported previously[28]) and are consistent with the TEM images.

Catalytic activity. NH_3 conversion and product selectivity of the reduced Pd catalysts during the operando XAFS/DRIFTS/mass spectrometry experiment were calculated from *m/z* signals of NH_3, N_2, NO, N_2O and NO_2 (*m/z* = 17, 28, 30, 44 and 46) relative to the inlet NH_3 signal, and are plotted in Fig. 1 for Pd/γ-Al_2O_3 and Pd/zeolite- Y. Both catalysts exhibit similar catalytic activity, achieving 50% NH_3 conversion at 213 °C (1.5 wt% Pd/γ-Al_2O_3) and 190 °C (1.5 wt% Pd/zeolite-Y), which is close to that reported previously[15]. The product selectivity to dinitrogen and nitrogen oxides at increasing temperature can be described by three distinct temperature regions: $150\ °C < T_1 < 240\ °C$, $240\ °C < T_2 < 300\ °C$ and $300\ °C < T_3 < 400\ °C$. The low-temperature regime, T_1, showed a period of high selectivity to N_2.

During the mid-temperature region T_2, N_2 formation reached a plateau and the formation of N_2O increased steadily. The start of the high-temperature region T_3 was defined by an onset of NO forma-tion and a decrease in N_2O formation. Due to the similar properties of both Pd nanoparticle catalysts in this study, only the results from the Pd/γ-Al_2O_3 catalyst will be discussed hereafter (the results from Pd/zeolite-Y are shown in the Supplementary Information).

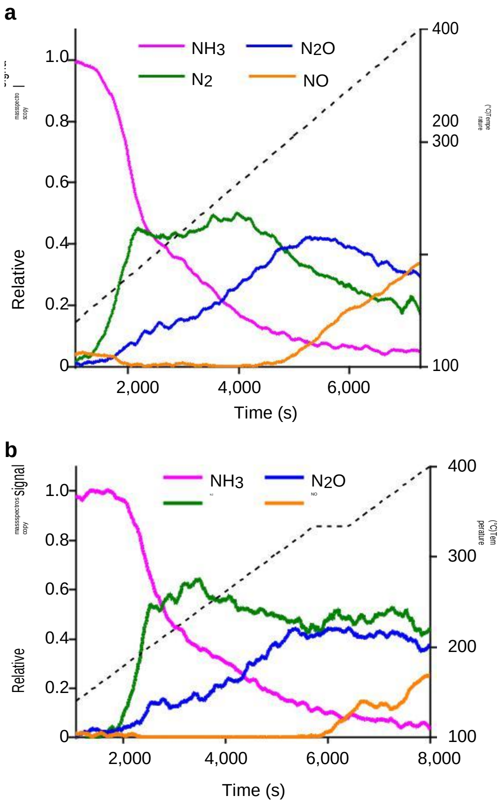

Fig. 1 | Catalytic activity of supported Pd catalysts for NH_3 oxidation at increasing temperatures. a, 1.5 wt% Pd/zeolite-Y. **b**, 1.5 wt% Pd/γ-Al_2O_3. Reactant gas feed: 0.5% NH_3; 2.5% O_2; 97% He. Dashed line, catalyst temperature.

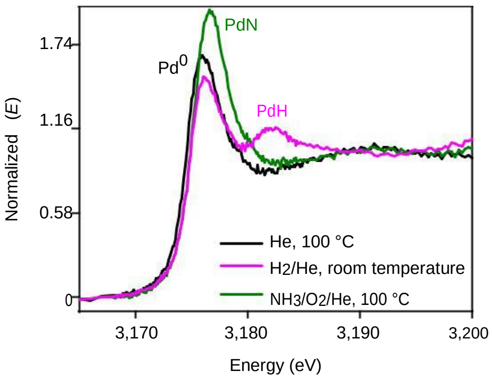

Fig. 2 | In situ Pd L_3-edge XANES spectra of 1.5 wt% Pd/γ-Al_2O_3 in different gas environments. XANES spectra collected after in situ reduction in H_2 at 200 °C, then exposure to inert helium at 100 °C (black), 10% H_2 at room temperature (magenta) or 0.5% NH_3, 2.5% O_2 and helium at 100 °C (green). Normalized $\mu(E)$ is the normalized absorption.

Pd L_3-edge XANES. In situ Pd L_3-edge XANES was performed to determine the Pd electronic structure during NH_3 and O_2 reaction conditions at low temperature. The Pd L_3-edge XANES results of Pd/γ-Al_2O_3 are shown in Fig. 2 before and after switching to an NH_3 and O_2 atmosphere, together with a reference spectrum of palladium hydride collected by cooling the sample to room temperature in 5% H_2/He. Palladium hydride gives rise to a distinct absorption feature at 3,182 eV due to excitation of 2*p* electrons to a Pd–H antibond-ing state (Fig. 2)[29–31]. The XANES spectrum of Pd/γ-Al_2O_3 collected under helium at 100 °C, after a reduction pre-treatment (Fig. 2), is

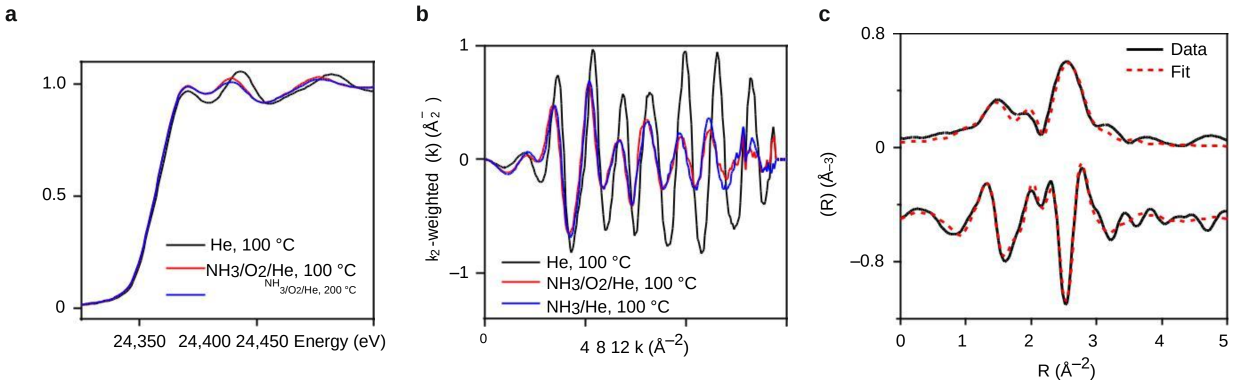

Fig. 3 | Operando Pd K-edge XANES and EXAFS spectra of Pd/γ-Al_2O_3 under different reaction conditions. a, Pd K-edge XANES spectra of 1.5 wt% Pd/γ-Al_2O_3 after reduction pre-treatment in H_2, then exposure to helium at 100 °C (black), 0.5% NH_3, 2.5% O_2 and helium at 100 °C (red) or 0.5% NH_3, 2.5% O_2 and helium at 200 °C (blue). **b**, Pd K-edge k^2-weighted EXAFS of 1.5 wt% Pd/γ-Al_2O_3 after reduction pre-treatment, then exposure to helium (black), 0.5% NH_3, 2.5% O_2 and helium (red) or 0.5% NH_3 and helium (blue) at 100 °C. **c**, Stacked plot of the magnitude (top) and imaginary (bottom) non-phase corrected Fourier-transformed Pd K-edge EXAFS of 1.5 wt% Pd/γ-Al_2O_3 at 100 °C under an atmosphere of 0.5% NH_3, 2.5% O_2 and helium, plotted with the fit constructed from Pd–N and Pd–Pd scattering paths.

consistent with that of Pd foil for the metallic Pd^0 oxidation state. After switching to the reactant (NH_3 and O_2) gas feed at 100 °C, the Pd L_3-edge XANES spectra show increased intensity and broadening of the white line (Fig. 2), but without the characteristic absorption feature at 3,182 eV for palladium hydride.

The Pd L_3-edge XANES spectra confirm that there is a change to the Pd structure on introduction of the reactant (NH_3 and O_2) gas feed that cannot be attributed to the formation of palladium hydride. The increase in intensity and broadening of the white-line intensity of the Pd L_3-edge XANES spectra has previously been reported for the in situ formation of a carbide-like phase[22]. However, the absence of carbon in this system leads us to infer the formation of another type of interstitial structure, palladium nitride[32]. On repeating this procedure with a gas feed of 0.5% NH_3 and helium, the same result is obtained (Supplementary Fig. 6), showing that the same structural phase is also formed without the presence of O_2. Further evidence of the palladium nitride species was inferred from X-ray photoelectron spectroscopy (XPS) spectra of the sample after treating with NH_3 gas. Deconvoluting the peak in the nitrogen 1*s* region identifies the presence of two nitrogen species at 402 and 398 eV (Supplementary Fig. 7). The nitrogen 1*s* species located at 402 eV is consistent with NH_3 molecular species, whereas the species located at 398 eV is consistent with the formation of a reduced nitrogen, as in metal nitrides[32,33].

Operando Pd K-edge XAFS. The change in the electronic structure of the Pd species on exposure to the reactant NH_3, O_2 and helium gas feed is confirmed again by comparison of the Pd K-edge XANES spectra recorded before and after gas switching from inert to NH_3, O_2 and helium, as seen in Fig. 3a. On addition of the reactant NH_3, O_2 and helium gas feed, the near-edge features at 24,393 and 24,432 eV shifted by around 4 eV to lower energies. These observations could be reproduced by exposing the catalyst to a 0.5% NH_3 and helium gas feed (Supplementary Fig. 9). As oxygen is not required to impart the Pd structural change observed by XANES, we can rule out that these observations are a consequence of oxidation. Moreover, a surface oxidation would result in a different XANES spectrum from that observed, as shown in Fig. 4. The observed change in Pd K-edge XANES features has also been reported for heteroatom insertion inside the metal Pd face-centred cubic framework of supported Pd nanoparticles during in situ formation of a palladium carbide phase, suggesting similar structural and electronic changes to the Pd nanoparticles in this case[24,26]. These observations again support the proposed formation of an interstitial compound.

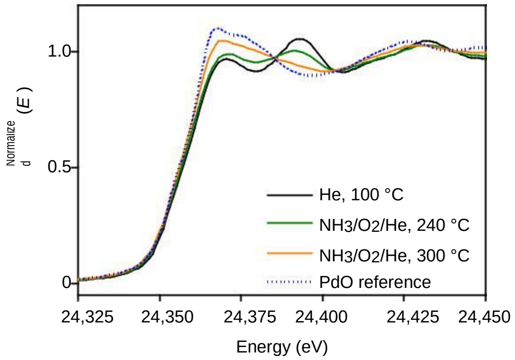

Fig. 4 | Operando Pd K-edge XANES spectra of 1.5 wt% Pd/γ-Al_2O_3 under different reaction conditions. Pre-treatment in H_2, then exposure to helium at 100 °C (black), 0.5% NH_3, 2.5% O_2 and helium at 240 °C (green) or 0.5% NH_3, 2.5% O_2 and helium at 300 °C (orange). The Pd K-edge XANES spectrum of bulk PdO under ambient conditions is shown as a reference (blue, dashed).

The Pd K-edge extended XAFS (EXAFS) spectra give information on the average local atomic environment of the absorbing Pd atoms in the sample. Major disruption to the local atomic arrangement of the metallic Pd nanoparticles on introduction of the NH_3 and O_2 reactant gas mixture (and NH_3/He only) can be observed as a decreased amplitude and phase shift of the k^2-weighted Pd K-edge EXAFS oscillations, as seen in Fig. 3b, which shows that there must be substantial heteroatom insertion not only to cause expansion of the face-centred cubic lattice, but also to cause significant disruption of the local atomic ordering. The Fourier-transformed EXAFS spectrum (Fig. 3c) can be fitted with a model using first-shell coordination to nitrogen ($R_{\text{Pd–N}}$ = 2.00 Å) and a second shell coordination to palladium ($R_{\text{Pd–Pd}}$ = 2.81 Å), with coordination numbers of 1 and 9.9, respectively (Table 1).

The Pd K-edge XANES spectra collected during the high-temperature NH_3 oxidation regime are plotted in Fig. 4. The spectrum collected at 240 °C (green) shows that the XANES features return to energies that resemble the initial Pd^0 spectrum collected under an inert atmosphere (black), but with a slight increase in white-line intensity and dampening of the metallic feature at 24,393 eV.

This flattening of the metallic feature and increase in white-line intensity can result from temperature differences, as well as partial oxidation of Pd^0 to Pd^{2+} due to PdO formation. Linear combination

Table 1 | Pd K-edge EXAFS fitting parameters of 1.5 wt% Pd/γ-Al_2O_3 at 100 °C in 0.5% NH_3, 2.5% O_2 and helium

Absorber - Scatterer	*N*	*R* (Å)	σ^2 (Å^2)	E_0 (eV)	R_{factor}
Pd–N	1.0 (2)	2.00 (1)	0.003 (2)	−5.7 (4)	0.02
Pd–Pd	9.9 (1)	2.810 (5)	0.0161 (8)		

Fitting parameters: $S_0^2 = 0.8$; fit range $3 < k$ (Å^{-2}) <10.6, $1 < R$ (Å) < 3; number of independent points =9.

fitting (detailed in Supplementary Table 3 and Supplementary Fig. 11) describes the Pd K-edge XANES collected at 240 °C as an approximate summation of ~40% Pd^0 and ~60% Pd^{2+} species. This fitting used the Pd K-edge XANES spectra collected at 100 °C in helium and at 300 °C in NH_3 and O_2 to represent Pd^0 and Pd^{2+} species of this particle size, respectively. The ratio of 40% Pd^0 and 60% Pd^{2+} is expected for a thin oxidic surface layer of supported Pd nanoparticles of approximately 2 nm diameter, as reported previously[34]. The greater ratio of Pd located at the surface of small nanoparticles has significant contribution to the averaged Pd signal of the measured XANES spectrum.

The Fourier-transformed EXAFS of the sample at 240 °C, shown in Supplementary Fig. 12, shows scattering features at 1.8 and 2.6 Å for first-shell Pd–O and Pd–Pd neighbours, respectively, but absence of a second-shell Pd–$Pd_{(2)}$ scattering feature related to a bulk Pd oxide, expected at 3.01 Å. These observations confirm that any Pd–O formation at 240 °C is short range and limited only to the Pd nanoparticle surface.

At temperatures beyond 240 °C, the white-line intensities of Pd K-edge XANES spectra increase further and metallic features diminish such that the XANES spectrum collected at 300 °C (orange; Fig. 4) resembles that of a bulk PdO phase. The Fourier-transformed Pd K-edge EXAFS spectra (Supplementary Fig. 12) show a major transition from a metallic nanoparticle structure at 240 °C to an oxide nanoparticle structure at 300 °C, and growth in amplitude of the oxide scattering features from 300–340 °C. The Fourier-transformed EXAFS of the sample at 340 °C can be fitted to a model using scattering paths of Pd–O ($R_{Pd–O} = 2.01$ Å), Pd–$Pd_{(1)}$ ($R_{Pd–Pd1} = 3.01$ Å) and Pd–$Pd_{(2)}$ ($R_{Pd–Pd2} = 3.455$ Å), with coordination numbers 3.7 (3), 1.0 (9) and 2 (2), respectively (Supplementary Fig. 13 and Supplementary Table 4).

Operando Pd K-edge XAFS have therefore identified three structural phases of Pd nanoparticles during NH_3 oxidation. The first is a PdN_x species that forms during the low-temperature regime (100 °C $\leq T_1 \leq$200 °C), where the main product of NH_3 oxidation is N_2. The second is a Pd nanoparticle with bulk metallic structure and a surface oxide that forms in the mid-temperature regime (240 °C $< T_2 <$300 °C), where an increasing amount of NH_3 is oxidized to N_2O. The third structural phase is a bulk PdO nanoparticle formed at high temperature ($T_3 >$300 °C), which is linked to the production of NO.

Operando DRIFTS. Figure 5 shows the difference DRIFTS spectrum of catalyst Pd/γ-Al_2O_3, collected simultaneously with the XAFS, after switching from inert helium to the reactant NH_3 and O_2 gas feed at 100 °C. The sharp bands between 1,250 and 1,600 cm^{-1} are typical of NH_3 adsorbed on surface acid sites. The bands at 1,596 and 1,256 cm^{-1} are assigned to asymmetric and symmetric deformation of coordinated ammonia, respectively[14–17]. The band at 1,450 cm^{-1} can be assigned to asymmetric deformation of ammonium ions adsorbed on Brønsted sites of the support[14,18–20], and the shoulder at 1,490 cm^{-1} can be assigned to NH_3 coordinated to Pd[11]. Low-intensity combination bands of ammonia and ammonia dimers may give rise to the broad band around 2,470 cm^{-1} (ref. 35). Absorption

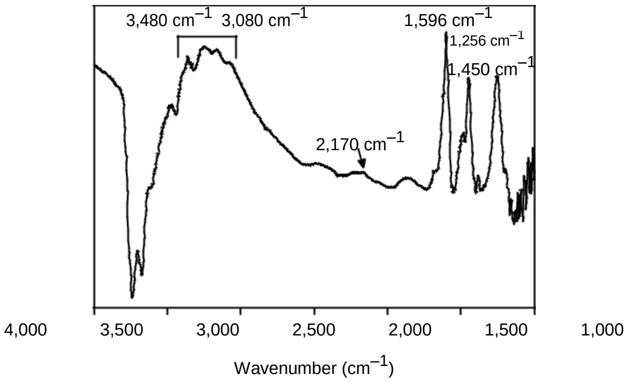

Fig. 5 | Operando DRIFTS spectrum of 1.5 wt% Pd/γ-Al_2O_3 during NH_3 oxidation. Difference DRIFTS spectrum showing the change from the spectrum collected after reduction pre-treatment in helium and that in 0.5% NH_3, 2.5% O_2 and helium reactant gas at 100 °C.

bands between 3,080 and 3,480 cm^{-1} are typical of symmetric and asymmetric N–H stretching of coordinated ammonia[36,37]. Negative bands above 3,500 cm^{-1} show the absence of O–H stretches due to NH_4^+ occupying surface hydroxyl Brønsted acid sites. The dissociative adsorption of ammonia on the Pd nanoparticle surface is shown by a weak band at 1,377 cm^{-1}, which is attributed to the –NH_2 scissoring frequency[12,38], usually coupled with the band at 1,596 cm^{-1}. The broad, low-intensity band at 1,850 cm^{-1} is attributed to small amounts of neutral and positively charged nitrosyl (NO^+) species adsorbed on Pd^0 (ref. 39). The broad band of small intensity at 2,170 cm^{-1} is present in the DRIFTS spectrum of both catalysts after switching to the NH_3 and O_2 reactant gas feed at 100 °C, and when switching to an NH_3 and helium atmosphere (Supplementary Fig. 14). Absorption bands at this wavenumber have previously been associated with the vibrational frequency of an asymmetric N–N bond of bridging N_2 in multinuclear metal–dinitrogen complexes[22]. The observation of vibrational bands near 2,200 cm^{-1} during NH_3 oxidation conditions are sometimes attributed to the N–N stretch of adsorbed N_2O species[40,41]. However, the absence of a corresponding N–O stretch for N_2O (expected at 1,262–1,220 cm^{-1}) and the absence of N_2O detected in mass spectrometry signals at 100 °C means that the band at 2,170 cm^{-1} cannot be assigned to N_2O species at this temperature. Similar vibrational bands at 2,170 cm^{-1} are observed in the DRIFTS spectrum of 1.5 wt% Pd/zeolite under analogous conditions (Supplementary Figs. 19 and 20) and are reported for NH_3 adsorption over an Ag/Al_2O_3 catalyst between 160 and 220 °C, which also cannot be attributed to N–N stretching of N_2O[37]. We propose that this low-intensity absorption band results from an asymmetric stretch of dinitrogen species at the catalyst surface, following the dissociated adsorption of ammonia molecules. An absorption band at 1,455 cm^{-1} due to –NH wagging at the sample surface decreases in intensity from 200 to 220 °C, followed by the formation of small-intensity bands at 1,418, 1,302 and 1,548 cm^{-1} (Supplementary Fig. 15) due to the formation of adsorbed nitrate species[37,42–44]. The intensities of these nitrate bands increase sharply at 280 °C, suggesting the onset of NO formation at the catalyst surface, which is then desorbed and detected in the mass spectrometer from 300 °C.

DFT + D3 calculations. To clarify how the presence of interstitial nitrogen atoms influence the Pd–Pd bond distances, DFT + D3 calculations were performed. These calculations were done in the Pd(111) system with 0.12, 0.23, 0.47, 0.70 and 1.39 wt% of interstitial nitrogen atoms (optimized structures shown in Supplementary Fig. 21), which showed that the average Pd–Pd distance in the vicinity of interstitial nitrogen atoms is ~2.83 Å. This is consistent with the lattice expansion observed by Pd K-edge EXAFS during nitrogen atom insertion under NH_3 and O_2 reaction conditions. The lateral and vertical Pd–Pd distances were found to be in the range of 2.83–2.85 Å and 2.80–2.83 Å, respectively, irrespective of the concentration of nitrogen atom insertion. The Pd–N distances were in the range 1.91–1.99 Å, which is in agreement with the distances found from the Pd K-edge EXAFS data. Before relaxation, the interstitial N-atoms in all of the above models were set in the range 2.39–2.47 Å from each other. After relaxation the interstitial N-atoms moved by a distance approximately in the range 3.03– 3.34 Å, with some of the nitrogen atoms moving closer to the surface. The diffusion barrier for an interstitial nitrogen atom to move from an octahedral interstitial site to a surface threefold hollow was low (0.25 eV), suggesting that interstitial nitrogen atoms are able to diffuse to the surface to participate in the catalytic mechanism.

The adsorption properties of NH_3 on the Pd(111) surface were considered with and without the presence of interstitial nitrogen atoms. The adsorption energies of NH_3 molecules close to the interstitial nitrogen atom were more favourable compared with away from it in the same system, and also compared with the pristine Pd(111) surface by ~0.156 eV (all calculated adsorption energies of NH_3 on the Pd(111) surface with and without interstitial nitrogen atoms are given in Supplementary Tables 6–8). This is due to the interaction of nitrogen *p* and palladium *d* molecular orbitals in the bonding region. For the pristine Pd(111) surface, the Pd d_{z^2} orbital interacts with the nitrogen *p* orbital. In contrast, in the case of a Pd(111) surface with an interstitial nitrogen atom, the Pd d_{z^2} and d_{yz} interact with the nitrogen *p* orbital, leading to a stronger bonding interaction between Pd atoms with NH_3 molecules, and there is also trace contribution from other *d* orbitals. From this analysis, we can conclude that the Pd(111) surface with interstitial nitrogen atoms would have greater coverage of adsorbed NH_3 compared with the pristine Pd(111) surface.

Discussion

Three distinct regions of catalytic activity are identified for NH_3 oxidation over supported Pd nanoparticle catalysts. During the low-temperature region (100 °C ≤ T_1 ≤200 °C), the Pd K-edge and Pd L_3-edge XANES show that the Pd structure experiences lattice expansion with insertion of nitrogen into the metallic Pd nanoparticle structure, which is confirmed by our DFT + D3 calculations. The dissociation of NH_3 during this temperature region is shown by $–NH_2$ wagging (at 1,377 cm^{-1}), $–NH_2$ scissoring (1,455 cm^{-1}) and a low-intensity vibrational band at 2,170 cm^{-1} for N–N stretching at the catalyst surface. The greater stability of NH_3 adsorption on the palladium nitride nanoparticle surface is calculated from molecular models and infers a high NH_3 surface coverage. Additionally, the low-energy barrier for diffusion of interstitial nitrogen to the surface indicates the ability for interstitial nitrogen to participate in the reaction mechanism by coupling with adsorbed NH_3 at the nanoparticle surface in a Mars–Van Krevelen-type mechanism. Indeed, a small contribution of *m/z* 28 for N_2 gas is detected by on-line mass spectrometry at 100 °C, which increases sharply at 150 °C in line with NH_3 conversion. By correlating the N–N surface species, Pd nanoparticle structure and N_2 formation (Supplementary Fig. 22) the N–N surface species are only observed when the Pd nanoparticles exist as PdN_x, and the desorption of such species coincides with the onset of N_2 formation. Following this, the contraction of the Pd distance—indicating the removal of interstitial nitrogen from the Pd lattice—is found to occur when N_2 formation exceeds 50%, relative to the inlet NH_3. This suggests the involvement of interstitial nitrogen in the reaction mechanism for the selective oxidation of NH_3 to N_2 (equation (1)), which is depleted when the rate of consumption is greater than the rate of replacement:

$$4NH_3 \quad 3O_2 \quad 2N_2 \quad 6H_2O \tag{1}$$

The active PdN_x nanoparticle structure is observed by operando Pd K-edge and Pd L_3-edge XANES up to 200 °C. At temperatures beyond 200 °C, the interstitial nitrogen is removed from the Pd lattice and the Pd K-edge XANES spectra show that the structure of the Pd nanoparticles returns to predominantly a metallic oxidation state, with a small oxidic surface layer. During this period, DRIFTS spectra show the presence of 2,240 and 2,210 cm^{-1} absorption bands for N_2O molecular vibrations beyond 180 °C, and there is an increase in N_2O gas reaching the mass spectrometer. Therefore, an increasing number of NH_3 molecules are oxidized to N_2O at the Pd surface, as per equation (2). The formation of N_2, as detected by mass spectrometry, can result from the NH_3-SCR reaction of adsorbed N_2O with incoming gaseous NH_3, as in equation (3)[45]:

$$2NH_3 + 2O_2 \quad N_2O + 3H_2O \tag{2}$$

$$2NH_3 \quad 3N_2O \quad 4N_2 \quad 3H_2O \tag{3}$$

Surface nitrate absorption bands are first observed in the DRIFTS spectra (as absorption bands at 1,418, 1,302 and 1,548 cm^{-1}) at 280 °C, and these increase significantly in intensity at higher temperatures. Nitrate formation at the catalyst surface correlates with the temperature for bulk oxidation of the Pd nanoparticles, as observed by a change in Pd K-edge XANES, and is followed by the onset of NO gas, as observed by mass spectrometry, at temperatures ≥300 °C. The complete oxidation of the Pd nanoparticles is confirmed by fitting the Pd K-edge EXAFS data collected at 340 °C to Pd–O and Pd–Pd paths of PdO. The over-oxidation of NH_3 to NO, by equation (4), has previously been attributed to high oxygen coverage at the precious metal surface, which prevents nitrogen coupling[23], but this study indicates that bulk oxide precious metal nanoparticles are the active catalytic species for NH_3 oxidation to NO above 280 °C:

$$4NH_3 \quad 5O_2 \quad 4NO \quad 6H_2O \tag{4}$$

The powerful combination of XAFS and DRIFTS, together with on-line mass spectrometry and DFT calculations, has allowed thorough characterization of the structure and surface reactivity of supported Pd nanoparticles during reaction for NH_3-SCO. The use of in situ Pd L_3-edge and operando Pd K-edge XAFS has identified a PdN_x species in the presence of an NH_3 and O_2 reactant gas feed that exists between 100 and 200 °C and is responsible for nitrogen coupling and dinitrogen formation in the direct oxidation pathway. During the mid-temperature range 240 °C < T_2 <300 °C, the catalyst comprises metallic Pd nanoparticles with a surface oxidic layer, which permits the formation of N_2 and N_2O. The formation of bulk PdO nanoparticles is achieved at higher temperatures (T_3 >300 °C), and coincides with the formation of nitrates at the catalyst surface and the onset of NO gas as a reaction product. Therefore, the selectivity of the catalytic NH_3 oxidation can be attributed to the Pd nanoparticle structure, with preferred selectivity to N_2 achieved from a previously unidentified PdN_x species. In contrast, the unfavourable over-oxidation to NO occurred at the surface of bulk PdO nanoparticles.

Methods

Sample preparation. Supported 1.5 wt% Pd catalysts were prepared by incipient wetness impregnation of an acidified aqueous solution of palladium nitrate (15.11 wt% Pd; Johnson Matthey) onto the commercial support: γ-Al_2O_3 (Sasol) and Zeolite Y (Zeolyst; CBV600, H-form, SiO_2/Al_2O_3 molar ratio of 5.2). Incipient wetness impregnation was carried out at room temperature. The impregnated supports were subsequently dried at 100 °C, then calcined in air at 500 °C for 2 h.

Ex situ characterization. TEM images of the samples were obtained using a JEOL JEM-2100 transmission electron microscope. Samples were prepared for TEM analysis by dispersing in high-purity ethanol using ultrasonication. Then, 10 µl of the sonicated suspension was pipetted onto a holey carbon-supporting copper grid, and the solvent evaporated. XPS analysis was performed with a Kratos AXIS Ultra DLD apparatus, equipped with a monochromated aluminium Kαradiation X-ray source, charge neutralizer and hemispherical electron energy analyser. During data acquisition, the chamber pressure was kept below 10^{-9} mbar. The spectra were analysed using the CasaXPS software package (http://www.casaxps.com/) and corrected for charging using the carbon 1*s* binding energy as the reference at 284.8 eV.

Operando Pd L_3-edge XANES. Operando Pd L_3-edge XANES (3,175 eV) were collected in fluorescence mode at the XMaS beamline of the European Synchrotron Radiation Facility. The catalyst sample (125–250 µm pellet fraction) was contained between two Kapton windows as a packed bed within a 100 µm trench of a flow reactor, as reported elsewhere[46]. The reactor was mounted within a helium chamber and connected to gas lines for flow of reactant gases to the sample. The effluent flow from the reactor was sent to a Hiden QGA mass spectrometer. The temperature was controlled by a thermocouple inserted close to the catalyst bed. The energy range (3,150–3,220 eV) was selected using a double-crystal Si(111) monochromator, and spectra were collected using a fluorescence detector at 90° to the X-ray beam and with the sample orientated at 45° to the incoming beam. Each scan measured 265 points with a counting time of 5 s per point, taking a total time of 22 min per spectrum. The experimental procedure consisted of online pre-treatment at 200 °C in a reducing (5% H_2 and helium) atmosphere. The reactant gas mixture was introduced (0.5% NH_3, 2.5% O_2 and 97% He) at 100 °C with a total flow of 40 ml min^{-1}, before ramping by 2.5 °C min^{-1} to 200 °C. The palladium hydride was formed in situ by cooling the sample to room temperature in 10% H_2 and helium. The palladium nitride was formed by introducing 0.5% NH_3 and helium to the reduced catalyst at 100 °C.

Operando Pd K-edge XAFS, DRIFTS and mass spectrometry. Operando XAFS and DRIFTS measurements were conducted at SuperXAS X10DA (Swiss Light Source, Paul Scherrer Institute) using a previously reported Harrick[47–49] DRIFTS cell integrated with an Agilent Carey 680 Fourier-transform infrared spectrometer. A DaVinci arm accessory fitted with praying mantis optics was used to refocus the infrared beam outside the Fourier-transform infrared spectrometer for positioning of the Harrick DRIFTS cell in the X-ray path. The Harrick DRIFTS cell has an X- ray path length of 3.17 mm through the sample positioned 1.04 mm below the surface of the catalyst bed. The experiment used a controlled flow of mixed gases into the reaction chamber under atmospheric pressure using Brooks mass flow controllers, and the temperature of the catalyst was controlled and monitored by a thermocouple positioned inside the catalyst bed. Each run used ~10 mg of pelletized (125–250 µm) catalyst. XAFS measurements were performed at the Pd K -edge (24,358 eV) in transmission mode using the QEXAFS setup with an oscillating Si(311) double-crystal monochromator operating at 1 Hz. All XAFS spectra were acquired with a Pd foil placed between I_t (the ion chamber detector after the sample) and I_r (the ion chamber detector placed after the reference), and the time resolution was 0.5 s per spectrum (k_{max} = 16.2). DRIFTS spectra were collected taking 64 scans with a resolution of 4 cm^{-1} using the liquid nitrogen cooled MCT detector. The time resolution of DRIFTS was 30 s per spectrum (400–4,000 cm^{-1}). At the same time, the composition of effluent gas was measured using a mass spectrometer (Hiden QGA) for H_2 ($m/z = 2$), helium ($m/z = 4$), NH_3 ($m/z = 17$), H_2O ($m/z = 18$), N_2 ($m/z = 28$), NO ($m/z = 30$), O_2 ($m/z = 32$), N_2O ($m/z = 44$) and NO_2 ($m/z = 46$). The experimental procedure consisted of online pre-treatment at 400 °C in a reducing (5% H_2 and helium) atmosphere, then cooling to 100 °C in helium. The reactant gas mixture was introduced (0.5% NH_3, 2.5% O_2 and 97% He) at 100 °C with a total flow of 40 ml min^{-1}, before ramping at 2.5 °C min^{-1} to 400 °C. Background DRIFTS spectra were recorded in flowing helium at 100 °C and subtracted from the sample spectrum for each measurement.

DFT + D3 calculations. All of the spin-polarized periodic density functional theory-based calculations were performed using the Vienna Ab Initio Simulation Package (VASP)[50–52]. The projector augmented wave method was used and the cut-off energy for the expansion of the plane-wave basis sets was set to 550 eV, which gave bulk energies converged to within 10^{-5} eV[53]. A convergence criterion of 0.01 eV $Å^{-1}$ was chosen for structural optimizations and a k-point grid of 3 × 3 × 1 was employed for all slab calculations. Benchmark calculations were used to check the results obtained with Monkhorst–Pack k-point grids of different grid densities, as detailed in Supplementary Note 1, which gave negligible differences in calculated adsorption energies (Supplementary Table 9) . We used a smearing value of 1 (which is recommended in the VASP manual to be appropriate for metals[54]) and a partial occupancy value of 0.2 eV. Benchmark calculations were used (detailed in Supplementary Note 2) to check the influence of the partial occupancy value on the calculated adsorption energies (Supplementary Table 10). The Perdew–Burke–Ernzerhof version of generalized gradient approximation was used to carry out geometry optimizations and total energy calculations[55]. The ideal Pd(111) surfaces were modelled by a 2 × 2 cell with 7 atomic layers. For calculations involving the adsorption of NH_3, the bottom four of the seven atomic layers were fixed to mimic the bulk of the material. The slabs were cut from bulk Pd with a calculated energy minimized lattice constant of 3.904 Å (which compares well with the experimental value of 3.891 Å) while in the direction perpendicular to the surface, a vacuum gap of ~15 Å was used. To check the increase in the Pd–Pd distances due to the presence of interstitial nitrogen atoms, a series of calculations were performed by systematically increasing the number of nitrogen atoms at the interstitial positions. For all of these calculations, we placed the interstitial nitrogen atoms at the centre of the octahedral sites that are close to both the exposed surfaces, and relaxed the atomic coordinates within a fixed cell. This study was extended to clarify the influence of the interstitial nitrogen atoms on the adsorption properties of NH_3 molecules on the Pd(111) surface. The adsorption of NH_3 molecules was allowed on only one of the two exposed surfaces. The dipole moment, due to the adsorbed species, was taken into account using the methods implemented in VASP according to the procedures of Makov et al.[56] and Neugebauer et al.[57] . In this study, we also employed Grimme's dispersion correction (DFT + D3), as dispersive effects might be significant for such systems[58] . The climbing-image nudged elastic band method was employed to determine the minimum energy path for evaluating the activation energy barrier for the diffusion of interstitial nitrogen atoms[59,60].

Data availability

The data that support the findings of this study are available from the University of Southampton repository with the identifier https://doi.org/10.5258/SOTON/ D0709, or from the authors upon reasonable request.

Received: 13 April 2018; Accepted: 10 December 2018;
Published online: 28 January 2019

References

\1.\Sobczyk, D. P., Hensen, E. J. M., de Jong, A. M. & van Santen, R. A. Low-temperature ammonia oxidation over Pt/γ-alumina: the influence of the alumina support. *Top. Catal.* **23**, 109–117 (2003).

\2.\ Weststrate, C. J., Bakker, J. W., Gluhoi, A. C., Ludwig, W. & Nieuwenhuys, B. E. Ammonia oxidation on Ir(1 1 1): why Ir is more selective to N_2 than Pt. *Catal. Today* **154**, 46–52 (2010).

\3.\Hung, C.-M. Characterization and performance of Pt–Pd–Rh cordierite monolith catalyst for selectivity catalytic oxidation of ammonia. *J. Hazard. Mat.* **180**, 561–565 (2010).

\4.\Gang, L., Anderson, B. G., van Grondelle, J. & van Santen, R. A. Low temperature selective oxidation of ammonia to nitrogen on silver-based catalysts. *Appl. Catal. B* **40**, 101–110 (2003).

\5.\Burch, R. & Southward, B. W. L. The nature of the active metal surface of catalysts for the clean combustion of biogas containing ammonia. *J. Catal.* **198**, 286–295 (2001).

\6.\ Carabineiro, S. A. C., Matveev, A. V., Gorodetskii, V. V. & Nieuwenhuys, B. E. Selective oxidation of ammonia over Ru(0 0 0 1). *Surf. Sci.* **555**, 83–93 (2004).

\7.\Carabineiro, S. A. C. & Nieuwenhuys, B. E. Selective oxidation of ammonia over Ir(5 1 0). Comparison with Ir(1 1 0). *Surf. Sci.* **532–535**, 87–95 (2003).

\8.\Qi, G., Gatt, J. E. & Yang, R. T. Selective catalytic oxidation (SCO) of ammonia to nitrogen over Fe-exchanged zeolites prepared by sublimation of $FeCl_3$. *J. Catal.* **226**, 120–128 (2004).

\9.\Qi, G. & Yang, R. T. Selective catalytic oxidation (SCO) of ammonia to nitrogen over Fe/ZSM-5 catalysts. *Appl. Catal. A* **287**, 25–33 (2005).

\10.\ Long, R. Q. & Yang, R. T. Superior ion-exchanged ZSM-5 catalysts for selective catalytic oxidation of ammonia to nitrogen. *Chem. Commun.* **0**, 1651–1652 (2000).

\11.\Gang, L., van Grondelle, J., Anderson, B. G. & van Santen, R. A. Selective low temperature NH_3 oxidation to N_2 on copper-based catalysts. *J. Catal.* **186**, 100–109 (1999).

\12.\Chmielarz, L., Kuśtrowski, P., Rafalska-Łasocha, A. & Dziembaj, R. Selective oxidation of ammonia to nitrogen on transition metal containing mixed metal oxides. *Appl. Catal. B* **58**, 235–244 (2005).

\13.\Lee, S. M. & Hong, S. C. Promotional effect of vanadium on the selective catalytic oxidation of NH_3 to N_2 over Ce/V/TiO_2 catalyst. *Appl. Catal. B* **163**, 30–39 (2015).

\14.\Il'chenko, N. I. Catalytic oxidation of ammonia. *Russ. Chem. Rev.* **45**, 1119 (1976).

\15.\Chmielarz, L. & Jablonska, M. Advances in selective catalytic oxidation of ammonia to dinitrogen: a review. *RSC Adv.* **5**, 43408–43431 (2015).

\16.\Barbier, J. Jr, Oliviero, L., Renard, B. & Duprez, D. Catalytic wet air oxidation of ammonia over M/CeO_2 catalysts in the treatment of nitrogen-containing pollutants. *Catal. Today* **75**, 29–34 (2002).

\17.\Li, P., Zhang, R., Liu, N. & Royer, S. Efficiency of Cu and Pd substitution in Fe-based perovskites to promote N_2 formation during NH_3 selective catalytic oxidation (NH_3-SCO). *Appl. Catal. B* **203**, 174–188 (2017).

\18.\Lousteau, C., Besson, M. & Descorme, C. Catalytic wet air oxidation of ammonia over supported noble metals. *Catal. Today* **241**, 80–85 (2015).

\19.\Jabłońska, M. et al. Zeolite Y modified with palladium as effective catalyst for selective catalytic oxidation of ammonia to nitrogen. *J. Catal.* **316**, 36–46 (2014).

\20.\Li, Y. & Armor, J. N. Selective NH_3 oxidation to N_2 in a wet stream. *Appl. Catal. B.* **13**, 131–139 (1997).

\21.\Nilsson, J. et al. Chemistry of supported palladium nanoparticles during methane oxidation. *ACS Catal.* **5**, 2481–2489 (2015).

\22.\Tew, M. W., Janousch, M., Huthwelker, T. & van Bokhoven, J. A. The roles of carbide and hydride in oxide-supported palladium nanoparticles for alkyne hydrogenation. *J. Catal.* **283**, 45–54 (2011).

\23.\Khan, N. A., Shaikhutdinov, S. & Freund, H. J. Acetylene and ethylene hydrogenation on alumina supported Pd–Ag model catalysts. *Catal. Lett.* **108**, 159–164 (2006).

\24.\Tew, M. W., Nachtegaal, M., Janousch, M., Huthwelker, T. & van Bokhoven, J. A. The irreversible formation of palladium carbide during hydrogenation of 1-pentyne over silica-supported palladium nanoparticles: in situ Pd K and L_3 edge XAS. *Phys. Chem. Chem. Phys.* **14**, 5761–5768 (2012).

\25.\Zhang, L., Zhang, C. & He, H. The role of silver species on Ag/Al_2O_3 catalysts for the selective catalytic oxidation of ammonia to nitrogen. *J. Catal.* **261**, 101–109 (2009).

\26.\Bugaev, A. L. et al. In situ formation of hydrides and carbides in palladium catalyst: when XANES is better than EXAFS and XRD. *Catal. Today* **283**, 119–126 (2017).

\27.\Lin, C.-M. et al. Size-dependent lattice structure of palladium studied by X-ray absorption spectroscopy. *Phys. Rev. B* **75**, 125426 (2007).

\28.\Beale, A. M. & Weckhuysen, B. M. EXAFS as a tool to interrogate the size and shape of mono and bimetallic catalyst nanoparticles. *Phys. Chem. Chem. Phys.* **12**, 5562–5574 (2010).

\29.\Soldatov, A. V., Della Longa, S. & Bianconi, A. Relevant role of hydrogen atoms in the XANES of Pd hydride: evidence of hydrogen induced unoccupied states. *Solid State Commun.* **85**, 863–868 (1993).

\30.\Ruckman, M. W. et al. XANES study of hydrogen incorporation in a Pd-capped Nb thin film. *Phys. Rev. B* **57**, 3881–3886 (1998).

\31.\Tew, M. W., Miller, J. T. & van Bokhoven, J. A. Particle size effect of hydride formation and surface hydrogen adsorption of nanosized palladium catalysts: L_3 edge vs K edge X-ray absorption spectroscopy. *J. Phys. Chem. C* **113**, 15140–15147 (2009).

\32.\Veith, G. M. et al. Evidence for the formation of nitrogen-rich platinum and palladium nitride nanoparticles. *Chem. Mater.* **25**, 4936–4945 (2013).

\33.\Briggs, D. Book Review: Handbook of X-ray spectroscopy. *Surf. Interface Anal.* **3**, 190 (1981).

\34.\Rogers, S. M. et al. Tandem site- and size-controlled Pd nanoparticles for the directed hydrogenation of furfural. *ACS Catal.* **7**, 2266–2274 (2017).

\35.\Wang, H. & Agmon, N. Complete assignment of the infrared spectrum of the gas-phase protonated ammonia dimer. *J. Phys. Chem. A* **120**, 3117–3135 (2016).

\36.\Liu, F. et al. Novel $MnWO_x$ catalyst with remarkable performance for low temperature NH_3-SCR of NO_x. *Catal. Sci. Technol.* **3**, 2699–2707 (2013).

\37.\Zhang, L. & He, H. Mechanism of selective catalytic oxidation of ammonia to nitrogen over Ag/Al_2O_3. *J. Catal.* **268**, 18–25 (2009).

\38.\Amores, J. G., Escribano, V. S., Ramis, G. & Busca, G. An FT-IR study of ammonia adsorption and oxidation over anatase-supported metal oxides. *Appl. Catal. B* **13**, 45–58 (1997).

\39.\Carré, S., Dujardin, C. & Granger, P. Operando infrared spectroscopy of the reduction of NO by H_2 over rhodium based catalysts. *Catal. Today* **191**, 59–64 (2012).

\40.\Zhanpeisov, N. U. et al. Interaction of N_2O with Ag^+ ion-exchanged zeolites: an FT-IR spectroscopy and quantum chemical ab initio and DFT studies. *J. Mol. Catal. A* **201**, 237–246 (2003).

\41.\Wcław, A., Nowińska, K., Schwieger, W. & Zielińska, A. N_2O decomposition over iron modified zeolites ZSM-5. *Catal. Today* **90**, 21–25 (2004).

\42.\Zhang, X., He, H., Gao, H. & Yu, Y. Experimental and theoretical studies of surface nitrate species on Ag/Al_2O_3 using DRIFTS and DFT. *Spectrochim. Acta A* **71**, 1446–1451 (2008).

\43.\Müslehiddinoğlu, J. & Vannice, M. A. Adsorption of NO on promoted $Ag/\alpha\text{-}Al_2O_3$ catalysts. *J. Catal.* **217**, 442–456 (2003).

\44.\Underwood, G. M., Miller, T. M. & Grassian, V. H. Transmission FT-IR and Knudsen cell study of the heterogeneous reactivity of gaseous nitrogen dioxide on mineral oxide particles. *J. Phys. Chem. A* **103**, 6184–6190 (1999).

\45.\Caravaggio, G., Nossova, L. & Burich, R. Influence of supports on Pd catalysts for the selective catalytic reduction of $NO_x$with H_2 and CO. *Emiss. Control Sci. Technol.* **2**, 10–19 (2016).

\46.\Thompson, P. B. J. et al. X-ray spectroscopy for chemistry in the 2-4 keV energy regime at the XMaS beamline: ionic liquids, Rh and Pd catalysts in gas and liquid environments, and Cl contamination in [gamma]-Al_2O_3. *J. Synchotron. Radiat.* **22**, 1426–1439 (2015).

\47.\Gibson, E. K. et al. Restructuring of AuPd nanoparticles studied by a combined XAFS/DRIFTS approach. *Chem. Mater.* **27**, 3714–3720 (2015).

\48.\Dann, E. K. et al. Combined in situ XAFS/DRIFTS studies of the evolution of nanoparticle structures from molecular precursors. *Chem. Mater.* **29**, 7515–7523 (2017).

\49.\Marinkovic, N. S. et al. Combined in situ X-ray absorption and diffuse reflectance infrared spectroscopy: an attractive tool for catalytic investigations. *Nucl. Instrum. Methods Phys. Res. A* **649**, 204–206 (2011).

\50.\Kresse, G. & Hafner, J. Ab initio molecular dynamics for liquid metals. *Phys. Rev. B* **47**, 558–561 (1993).

\51.\Kresse, G. & Hafner, J. Ab initio molecular-dynamics simulation of the liquid-metal–amorphous-semiconductor transition in germanium. *Phys. Rev. B* **49**, 14251–14269 (1994).

\52.\Kresse, G. & Furthmüller, J. Efficient iterative schemes for ab initio total-energy calculations using a plane-wave basis set. *Phys. Rev. B* **54**, 11169–11186 (1996).

\53.\Blöchl, P. E. Projector augmented-wave method. *Phys. Rev. B* **50**, 17953–17979 (1994).

\54.\Kresse, G., Marsman, M. & Furthmuller, J. Vienna ab initio simulation package (VASP) https://cms.mpi.univie.ac.at/vasp/vasp.pdf (2018)

\55.\Perdew, J. P., Burke, K. & Ernzerhof, M. Generalized gradient approximation made simple. *Phys. Rev. Lett.* **77**, 3865–3868 (1996).

\56.\Makov, G. & Payne, M. Periodic boundary conditions in ab initio calculations. *Phys. Rev. B* **51**, 4014–4022 (1995).

\57.\Neugebauer, J. & Schefer, M. Adsorbate–substrate and adsorbate–adsorbate interactions of Na and K adlayers on Al(111). *Phys. Rev. B* **46**, 16067–16080 (1992).

\58.\Grimme, S., Antony, J., Ehrlich, S. & Krieg, H. A consistent and accurate ab initio parametrization of density functional dispersion correction (DFT-D) for the 94 elements H-Pu. *J. Chem. Phys.* **132**, 154104 (2010).

\59.\Henkelman, G., Uberuaga, B. P. & Jónsson, H. Climbing image nudged elastic band method for finding saddle points and minimum energy paths. *J. Chem. Phys.* **113**, 9901–9904 (2000).

\60.\Henkelman, G. & Jónsson, H. Improved tangent estimate in the nudged elastic band method for finding minimum energy paths and saddle points. *J. Chem. Phys.* **113**, 9978–9985 (2000).

Acknowledgements

We acknowledge UCL and the EPSRC for the iCASE studentship of E.K.D; the beamline scientists at the Swiss Light Source and staff at the Paul Scherrer Institut for the provision of beamtime (proposal 20160396); and the beamline scientists at XMaS, European Synchrotron Radiation Facility, for the provision of beamtime (experiment 28-01-1213). XMaS is a UK national facility supported by EPSRC. We recognize staff at the University of Warwick and University of Liverpool for support in facilitating the beamtime. We also acknowledge the RCaH for the use of facilities, and Johnson Matthey for providing catalyst precursor materials and testing facilities. We thank the UK Catalysis Hub for resources and support provided via our membership of the UK Catalysis Hub Consortium (portfolio grants EP/K014706/1, EP/K014668/1, EP/K014854/1, EP/K014714/1 and EP/I019693/1). Via our membership of the UK's HEC Materials Chemistry Consortium, which is funded by the EPSRC (EP/L000202), this work used the ARCHER UK National Supercomputing service (http://www.archer.ac.uk). We acknowledge the use of Athena at HPC Midlands+, which was funded by the EPSRC (grant EP/P020232/1), in this research, via the EPSRC RAP call of spring 2018. We also thank HPC Wales for the computing time.

Author contributions

The experiments on SuperXAS were performed by P.P.W., E.K.D., E.K.G., R.H.B., M.N. and A.G. The experiments on XMaS at the European Synchrotron Radiation Facility were performed by P.P.W., E.K.D., G.F.T., P.T. and S.M.R. The catalysts were prepared by E.K.D. and A.R., with routine characterization performed by E.K.D. The X-ray absorption spectroscopy data were interpreted by P.P.W., E.K.D., A.K. and E.K.G. XPS measurements were performed and analysed by E.K.D., S.F.R.T. and T.E.E. The computational work was performed by A.C. and C.D.Z.-Y. The work was conceived and designed by P.P.W., C.R.A.C., A.G., P.C. and C.H. The manuscript was written by P.P.W., E.K.D., A.C. and A.G.

Competing interests

The authors declare no competing interests.

Additional information

Correspondence and requests for materials should be addressed to A.G. or P.P.W.